



POLITECNICO
MILANO 1863

SCUOLA DI INGEGNERIA INDUSTRIALE
E DELL'INFORMAZIONE

PROJECT REPORT - AERODYNAMICS OF TRANSPORT VEHICLES

Chassis and Spoiler Aerodynamics in Legends Car Racing

Authors: MATTEO BAIO, GAIA LAPUCCI, LAURA LIVOTI, THOMAS MAGNI

Professors: PROF. ALEX ZANOTTI, PROF. PAOLO SCHITO

Assistant professor: ING. STEFANO NEGRI

Academic year: 2024-2025

1. Introduction

The Legends Cars are a 5/8-scale race cars styled after American automobiles from the 1930s and 1940s, built on a tubular chassis and powered by a motorcycle engine. All cars share identical mechanical specifications, aiming to keep low costs and promote fair competition based on driver skills. In the last years, this championship has gained popularity in Italy, with races now taking place on increasingly larger and more prestigious circuits. As a result, the average speeds reached by the cars during races have increased, making the slipstream effect more pronounced and effective.



Figure 1: Legends car race at Monza Circuit

The aim of this work is to study the aerodynamic differences between two of the most commonly used chassis configurations to evaluate any differences in their aerodynamic loads. Addition-

ally, the effect of adding a simple roof spoiler to reduce the drag will also be analyzed. All the results are carried out through detailed CFD simulations using the well established open source code *OpenFOAM*. Numerical data of the isolated cars are also compared with a tuft test executed on the real car.

2. Geometry

The Legends Cars versions to be investigated are the Sedan and the Coupé. As mentioned in the introduction, they share the same mechanical components, while the main differences are related to the bodywork of the vehicles, which has the greatest impact on aerodynamics. This is why two completely different geometries have to be developed for the numerical simulations.

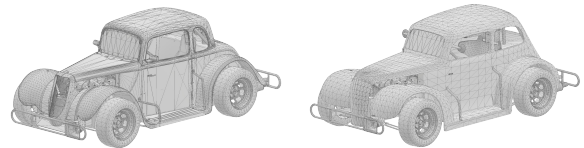


Figure 2: Original CAD models from Assetto Corsa: Coupé (left) and Sedan (right)

The preliminary CAD models shown in Figure 2 are optimized in accordance with the avail-

able computational power. This choice is supported by two main reasons. First of all, a simplified geometry facilitates the meshing process, resulting in a higher-quality mesh (with less distorted cells), together with reduced simulation time and lower computational cost. Additionally, it helps to gain a better understanding of the key flow phenomena to be investigated in this study.

It is crucial to specify that this approach affects the overall accuracy of the numerical outcomes, but not their consistency, as it is applied to both versions of the Legends Cars.

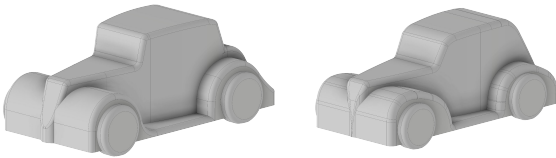


Figure 3: Simplified CAD models: Coupé (left) and Sedan (right)

The final configurations of the CAD models are shown in Figure 3. The CAD geometry reported above is developed using the software Autodesk Inventor, reproducing the shape of the .stl original versions of the Legends Cars in Figure 2.

The main differences between the real cars and the simplified models, as can be noticed comparing their images, are summarized as follows:

- Closure of cavities and air intakes: unnecessary setbacks avoided to ensure watertightness of the cars geometry.
- Flattening of the car underbody: the floor is modeled as flat as its detailed shape is not a primary focus of the study.
- Removal of external features: elements as side-view mirrors and front nerf bars have a negligible contribution on the aerodynamic performance of the simplified car.

3. CFD Methodology

As anticipated in the introduction, all the numerical simulations presented in this study are performed using *OpenFOAM* [1], an open-source software for computational fluid dynamics based on the solution of the Reynolds-Averaged Navier-Stokes (RANS) equations. Specifically, the steady-state solver *simpleFoam* (Semi-

Implicit Method for Pressure Linked Equations) is employed, which is suitable for incompressible turbulent flow simulations. To ensure high-fidelity results, particular attention must be paid to the meshing phase. The mesh is generated using *snappyHexMesh*, an internal tool of the above-mentioned software, which creates mesh elements starting from the outer farfield region towards the body, employing high-quality tetrahedral-dominant 3D elements.

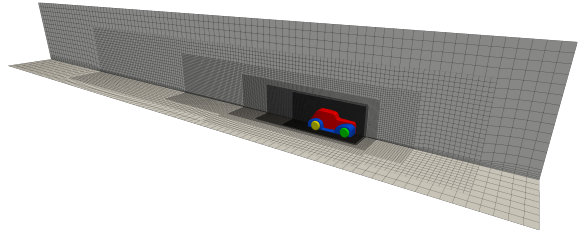


Figure 4: Domain refinement boxes

In Figure 4, the position of the car relative to the domain box (45m x 4m x 6m) can be seen. Wall distances are based on the method described by Qin et al. [2] to avoid boundary effects.

This figure also shows the presence of five different refinement boxes. They are strategically placed after the identification of the wake regions in the two bodywork configurations, aiming to better catch the interaction between the body and freestream air.

Specifically, the *snappyHexMesh* utility is used, following an octree-based mesh refinement approach. A level 5 refinement is imposed over the surface of the car, matching the volumetric refinement level of the first box. This consistency ensures a smooth transition in cell sizes, which is essential for accurately capturing boundary layer effects through the inflation layer, and helps prevent mesh distortions in critical zones of the geometry.

The mesh quality is iteratively checked during its generation process, dealing with parameters such as intersections, skewness and aspect ratio, so that the CFD solver is in favorable position to reach convergence.

To ultimately validate that the generated mesh is well suited for the case study, a grid independence analysis will be discussed in Section 4.1.

Once the domain is prepared, it is possible to proceed with the configuration of the numerical simulation. Second-order schemes are employed

in order to increase the accuracy of the results. Relevant boundary conditions used are reported in Table 1, while the different parts of the domain can be observed in Figure 5.

Region	Condition
Inlet	Fixed speed U_∞
Top, Right, Outlet	Freestream
Left	Symmetry
Bottom	Moving wall U_∞
Chassis	No slip
Tyres	Rotating wall ω_∞

Table 1: Boundary conditions applied to the domain

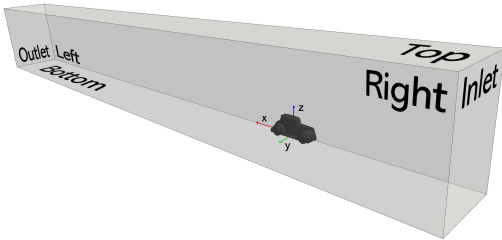


Figure 5: Domain boundary box

It is important to note that the exposed position of the wheels—both below the underbody and laterally—requires the usage of a *rotating wall* boundary condition to better capture the interaction between the tyres and the air, and consequently, the wake generated. Although previous images and final results are presented for the full car model, each simulation is performed by taking advantage of the problem symmetry.

Table 2 shows the initial flow conditions and geometrical parameters used to set up the numerical simulations. In particular, the freestream velocity is selected to ensure that the Reynolds number reaches the minimum value required for the onset of relevant aerodynamic effects. The turbulent kinetic energy and frequency are computed using the formulas provided in the *OpenFOAM User Guide* [3].

Among all the available turbulence models, the 2-equations $k-\omega$ SST guarantees an improved numerical stability, integrating the strengths of the $k-\epsilon$ model for resolving the outer wake region and of the $k-\omega$ model for capturing the inner boundary layer region, with a smooth transition

Parameter	Value
Freestream velocity, U_∞	17.5 m/s
Tyres angular speed, ω_∞	60.34 rad/s
Relative pressure, P_{rel}	0 Pa
Reynolds number, Re	2.6497×10^6
Air density, ρ	1.225 kg/m ³
Turbulent kin. energy, k	0.0459 m ² /s ²
Turbulent frequency, ω	0.6329 rad/s
Kinematic viscosity, μ	1.5×10^{-5} N s/m
Wheelbase length, L_c	1.854 m
Sedan frontal area, A_{ref}^S	0.665 m ²
Coupé frontal area, A_{ref}^C	0.645 m ²

Table 2: Main parameters used in CFD simulations

between the two models [4]. The choice is reinforced by the fact that a bluff body is being simulated.

This setup is further refined through the application of *wall functions*, which model the viscous sublayer—instead of resolving it directly (which would require $y^+ < 1$)—thereby saving computational resources. It is important to note that this simplification must be taken into account when extruding the inflation layer, to ensure y^+ values remain within the range of 30 to 300.

Finally, Figure 6 illustrates the division of the simulated half vehicle into multiple *patches*, along with the surface mesh surrounding it and the inflation layer. All these considerations are applied to both vehicles.

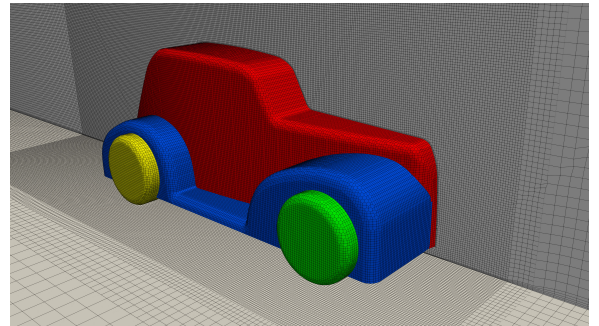


Figure 6: Surface mesh and *patches*

4. Numerical Results

The post-processing of the simulations is done with *ParaView*.

4.1. Grid and Farfield Convergence

To ensure the reliability of the numerical results, a grid independence study is performed alongside a farfield convergence study for both vehicles. The outcomes of these analyses, presented in terms of lift coefficient (C_L), drag coefficient (C_D), and their corresponding percentage errors, are shown in Figures 7 and 8, respectively.

From the grid convergence study (Figure 7), which is conducted using three levels of uniform mesh refinement (1.9M, 3.4M, and 6.5M cells), it can be concluded that the selected mesh consists of approximately 3.4×10^6 cells.

The farfield convergence study is performed by varying the length of the computational domain in the slipstream direction (35 m, 45 m, and 55 m) while maintaining the same mesh parameters used in the grid convergence study. Based on the farfield study (Figure 8), a domain length of 45 m is selected.

Convergence is achieved after 2500 iterations, with final residuals on the order of 10^{-5} . The aerodynamic coefficients are averaged over the last 500 iterations. Their values, shown in the following section, are consistent with those found in literature for this type of vehicles [5].

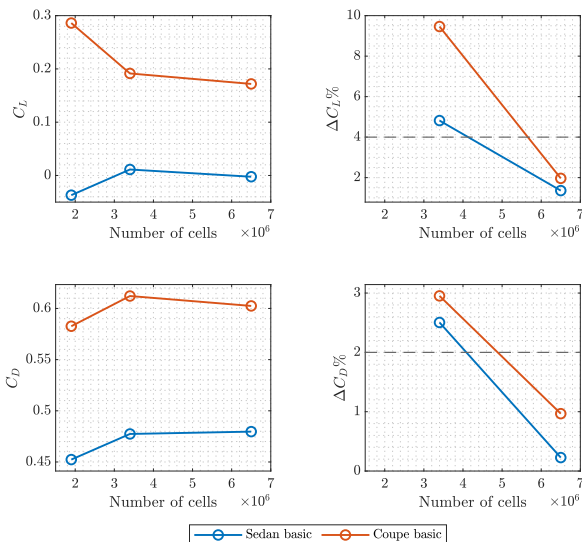


Figure 7: Grid convergence

4.2. Chassis Comparison

As already anticipated in the introduction, one of the goals of this study is to provide an aerodynamic comparison between the chassis of the Sedan and the Coupé models of Legends Cars. To do that, CFD simulations are performed with

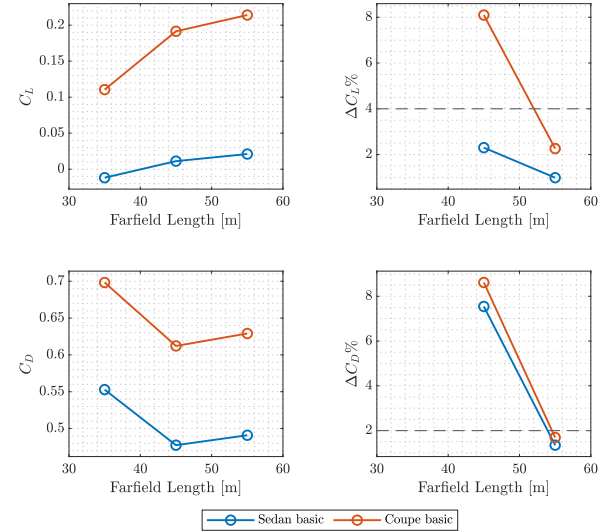


Figure 8: Farfield convergence

the numerical set-up described in Section 3 and the validated mesh (Section 4.1).

The comparison between the two models is assessed in terms of C_D and C_L , with a particular focus on the first coefficient. Tables 3 and 4 show the numerical results, highlighting the contribution of the isolated parts of each car to better understand where the aerodynamic differences may lay.

Patch	C_L	C_D	% of C_D
Upper Body	0.163	0.180	29.36%
Lower Body	0.018	0.379	61.98%
Front Tyre	0.012	0.022	3.66%
Rear Tyre	-0.002	0.031	5.00%
TOTAL	0.191	0.612	100%

Table 3: Coupé basic drag breakdown

Patch	C_L	C_D	% of C_D
Upper Body	0.014	0.102	21.44%
Lower Body	-0.011	0.323	67.69%
Front Tyre	0.010	0.021	4.31%
Rear Tyre	-0.001	0.031	6.56%
TOTAL	0.011	0.477	100%

Table 4: Sedan basic drag breakdown

First of all, the flow can be considered fully turbulent in both cases. This, combined with the bluff body shape of the car models, generally results in high values of drag coefficient. In par-

ticular, the Coupé chassis exhibits higher values of C_D and C_L . These differences are due to different flow field characteristics developed in the two cases.

The variation of the extent of the separation area behind the two car models represents the primary reason for the differences in their aerodynamic resistance. Figure 9 shows this region, which appears to be larger for the Sedan.

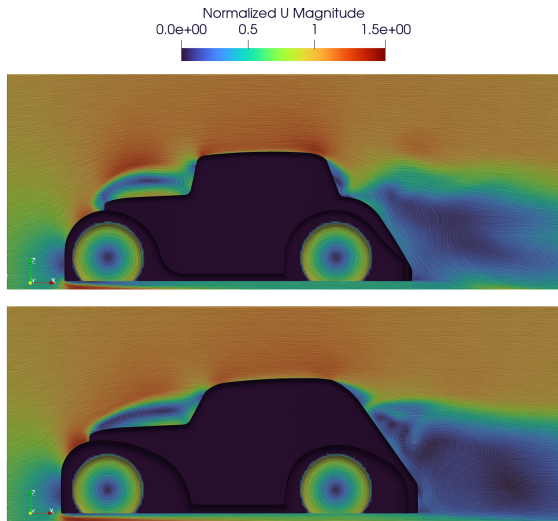


Figure 9: Coupé (top) and Sedan (bottom) LIC visualization with the normalized velocity field ($Y = 0.2$ m)

However, the following illustrations (Figure 11) will clearly highlight how the slipstream is populated with more vortical structures in the Coupé configuration.

With that in mind, *Q-criterion*, defined as the second invariant of the velocity gradient, is a useful quantity to highlight regions where vorticity is predominant. As a consequence, vortical structures can be observed by looking at the iso-surfaces of *Q-criterion*. Figure 10 shows the presence of separated regions also at the front of both vehicles. In particular, the flow separates at the cowl and then reattaches on the windshield forming a closed separation bubble. The vortex, rotating inside the bubble, exits at the sides and is drawn as longitudinal vortices. This is also visible in Figure 12. Figure 10 also highlights the presence of two vortices that originate from the upper part of the front tyres. The formation of these structures is a consequence of the wheels being exposed and contributes to an increase in pressure drag.

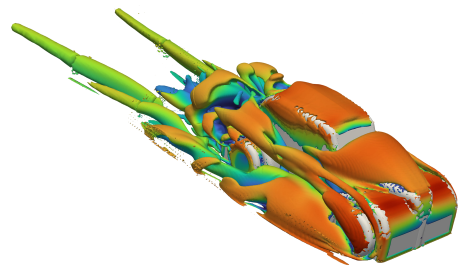
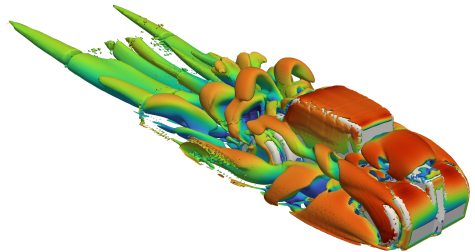
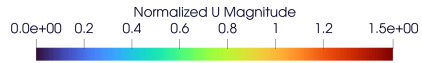


Figure 10: *Q-criterion* isosurfaces with the normalized velocity field: Coupé (top) and Sedan (bottom)

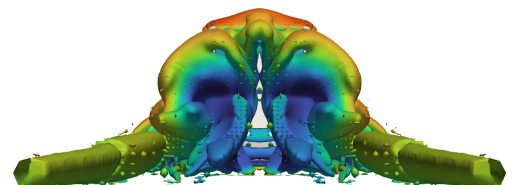
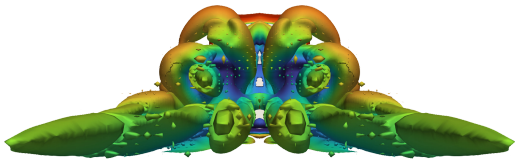
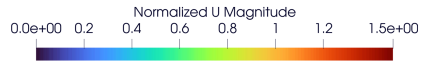


Figure 11: *Q-criterion* isosurfaces behind the vehicles with the normalized velocity field: Coupé (top) and Sedan (bottom)

On the other hand, Figure 11 shows the *C-pillar vortices* and puts into evidence the differences between the flow behaviour behind the two models. Having a higher slant angle, Coupé exhibits a much more chaotic wake with more vortical structures. Both wakes are made of counter-rotating vortices.

Figure 12 points out that the streamlines of the separation bubble on the Coupé chassis exhibit higher velocities. A possible explanation for this behavior lies in the (not directly visi-

ble) interaction between the bubble and the vortex shed from the front of the vehicle. This secondary phenomenon is not captured in the present results due to the well-known limitations of steady-state simulations when compared to unsteady approaches.

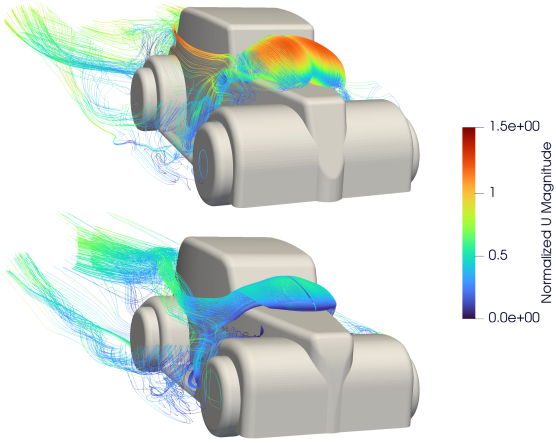


Figure 12: Streamlines visualization with the normalized velocity field: Coupé (top) and Sedan (bottom)

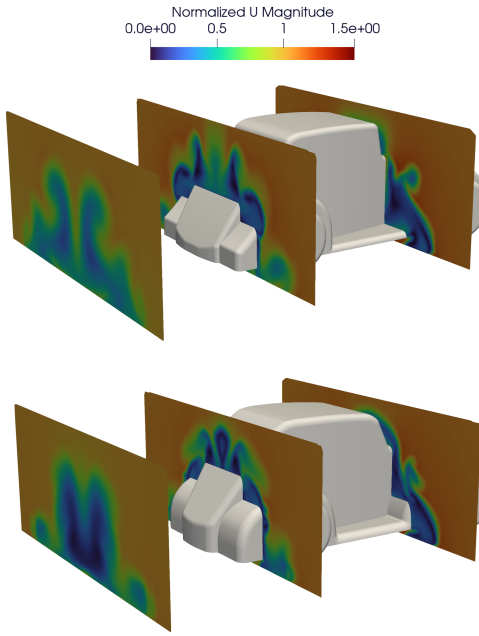


Figure 13: Slices with the normalized velocity field: Coupé (top) and Sedan (bottom)

Slices of the fluid domain and of the rear part of the vehicles shown in Figure 13 emphasize the vortical structures.

Figure 14 illustrates that the highest values of the static pressure coefficient C_{ps} are encountered

on the frontal part of the cars (stagnation area). The entirely vertical shape of the Coupé windshield contributes to a higher drag. Additionally, these cars generate positive lift, lacking a stabilizing effect in turning paths. The absence of high values of C_{ps} on the hood is one of the reasons why.

This is further confirmed by the distribution of the static pressure coefficient under the car, which does not show particularly low values (Figure 15). Figure 14, together with Figure 15, also shows another difference between the two chassis, confirmed by the values in Tables 3 and 4: Sedan Lower Body provides a downforce contribution, whereas the Coupé does not. In fact, the wheel arch region of the Coupé experiences a suction pressure effect, which counteracts downforce.

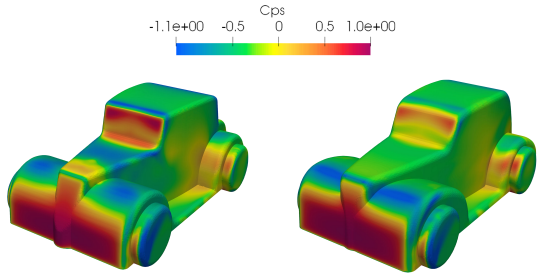


Figure 14: C_{ps} distribution: Coupé (left) and Sedan (right)

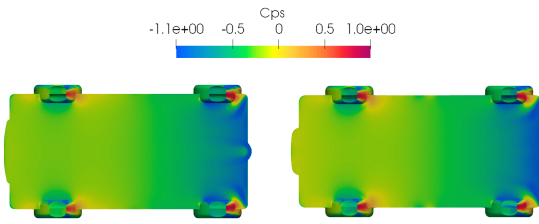


Figure 15: C_{ps} distribution beneath the car: Coupé (left) and Sedan (right)

4.3. Roof spoiler contribution

This section presents a study on drag reduction achieved through the addition of a strip-type roof spoiler. The detailed geometry of this element and its position on both cars are shown in Figure 16.

Based on the outcomes of a similar study conducted on the ahmed body [6], the spoiler pitch

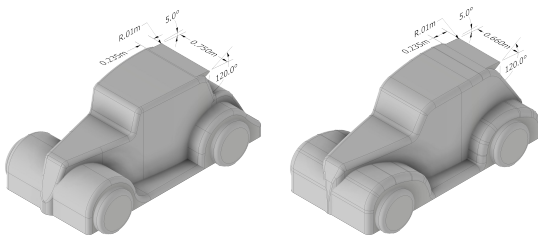


Figure 16: Simplified CAD models with spoiler: Coupé (left) and Sedan (right)

angle is selected to continue the roofline geometry. Furthermore, the spoiler design is based on the baseline flow field in order to ensure a delayed separation point. This design prioritizes drag reduction over increased downforce. The results of the analysis are reported in Tables 5 and 6.

Patch	C_L	C_D	% of C_D
Upper Body	-0.071	0.139	23.40%
Lower Body	0.016	0.391	65.84%
Front Tyre	0.015	0.024	4.01%
Rear Tyre	-0.009	0.029	4.92%
Spoiler	0.032	0.011	1.82%
TOTAL	-0.016	0.593	100%

Table 5: Coupé spoiler drag breakdown

Patch	C_L	C_D	% of C_D
Upper Body	-0.086	0.079	16.97%
Lower Body	-0.033	0.324	69.73%
Front Tyre	0.010	0.020	4.35%
Rear Tyre	-0.008	0.030	6.46%
Spoiler	0.027	0.012	2.49%
TOTAL	-0.090	0.465	100%

Table 6: Sedan spoiler drag breakdown

Predictably, the addition of the spoiler reduces the drag contribution especially on the Upper body, where the spoiler is located (as previously anticipated by the paper [6]). In fact, the flow is mainly altered near the end of the roof —where the spoiler is mounted— in both cases (as visible comparing Figures 9 and 17).

First of all, a noticeable separation bubble is formed just below the spoiler in both cases (as reported in the paper), causing a higher pressure zone that is mainly responsible for the drag

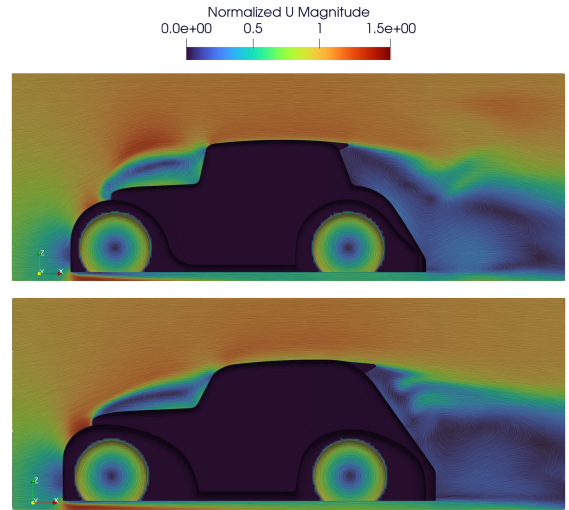


Figure 17: Coupé (top) and Sedan (bottom) with spoiler LIC visualization with the normalized velocity field ($Y = 0.2$ m)

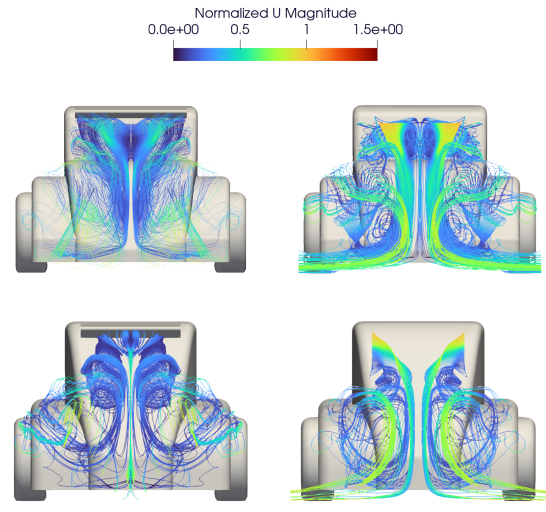


Figure 18: Coupé (top) and Sedan (bottom) with and without spoiler streamlines visualization with the normalized velocity field

reduction. This is supported by the presence of a slower wake —indicative of higher pressure— compared to the non-spoiler configuration, as revealed by the streamlines visualization (Figure 18). This figure also represents the key for visualising the separation bubbles. In the Coupé case, the bubble already present in the baseline configuration becomes larger and is positioned higher up. As for the Sedan chassis, the bubble appears only in the configuration with the spoiler. A small stationary bubble is actually present (Figure 19) in the Sedan baseline con-

figuration, but it does not interact with the vortices. In both cases, these separation regions change the way the flow behind the vehicles interacts with the vortices originating from the frontal area (Section 4.2). For example, in the Coupé case, the two vortical structures generated by the separation bubble merge with the two vortices originating from the sides of the car, in its lower region.

The drag reduction is more evident on the Coupé chassis compared to the Sedan one. This is clearly shown in the percentage reductions in Tables 5 and 6. In fact, as shown in Figure 18, it is evident that the separation bubble is larger in the Coupé case. The previously cited increased pressure behind the vehicles is also shown in Figure 19, where it is clear that the spoiler effect on the wake of the vehicle is stronger in the Coupé case.

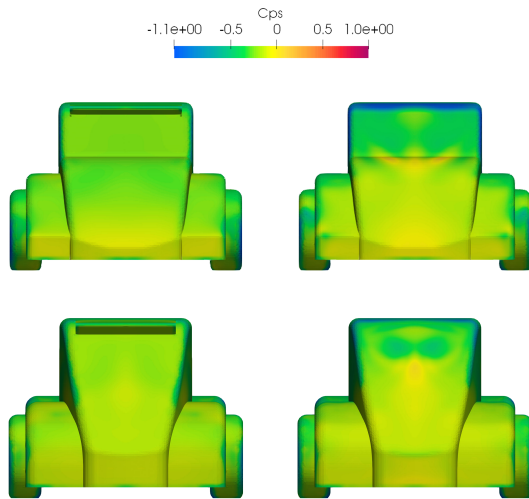


Figure 19: Coupé (top) and Sedan (bottom) with and without spoiler C_{ps} distribution behind the vehicle

The overall aerodynamic coefficient differences due to the spoiler addition are shown in Table 7, the C_D percentage reductions align well with the one foreseen in the paper (about 3 %).

Chassis	ΔC_L	ΔC_D	%dC_D
Coupé	-0.208	-0.019	3.08%
Sedan	-0.101	-0.012	2.53%

Table 7: Spoiler effect on aerodynamic loads

5. Experimental Study

In this last section, a *tuft test* is presented as an experimental study of the Legends Cars, aimed at validating some numerical outcomes of the CFD analyses.

5.1. Methodology and Setup

Tuft testing is commonly used in academic motorsports applications as one of the easiest and most cost-effective techniques for visualizing fluid flow phenomena over a car surface. It consists of the application of wool tufts on the car body, which respond to the local velocity, leading to intuitive conclusions regarding the flow field.

Thanks to the possibility of having two full-scale Legends cars available in a straight section of the *Castelletto Circuit*, this method is exploited to compare the real flow behavior with the one predicted during post-processing in *ParaView*. The two chassis are set up by applying a grid of tufts on the regions of interest. Due to the geometry simplifications described in Section 2, major discrepancies are expected in the lateral part of the bodywork. For this reason, the focus of the experimental study is to observe the flow field over the bonnets, wheel arches, windshields, rooftops and rear sections. As in the numerical study, only half of the cars is considered since the expected flow field is symmetric and no external factors, such as cross-wind or other cars wake, are present during the experiment. The left side is chosen for practical reasons related to the track configuration and sun position.



Figure 20: Tuft test setup in steady conditions

The length of the applied tufts is constant and approximately 70 mm. This value is chosen to ensure sufficient visibility while maintaining a size comparable to the characteristic length of the flow phenomenon. They are arranged in parallel rows spaced about 80 mm apart and staggered by approximately 60 mm to prevent tan-

gling between tufts even in separated flow regions.

Ultimately, the experiment is conducted at a constant GPS speed of 60 km/h, measured using the Aim MXM telemetry system integrated into Legends Cars. This ensures a Reynolds number very close to the one used in the numerical studies.

5.2. Experimental results

As the final stage of this work, Figures 21, 22, and 23 present the trackside acquisitions. Specifically, Figure 21 is a frame extracted from an onboard video, while the others are photographs taken from an external camera.

It is important to note that some tufts visible in the images are considered as outliers (red boxes), and should not be considered representative of the actual flow behavior discussed in the following analysis. A tuft is considered outliers if it is stacked with another one or if it stays still in multiple subsequent frame analyzed.

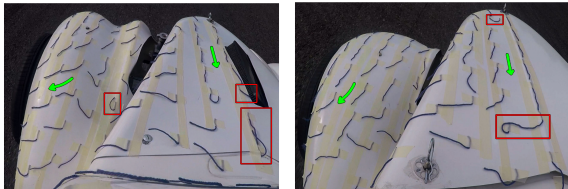


Figure 21: Onboard frame from the roof-mounted camera: Coupé (left) and Sedan (right)

Starting from the onboard views, both chassis configurations reveal a recirculation region ahead of the windscreens, which is consistent with the CFD results, though its extent appears smaller in the experimental images.

In Figure 21 a distinct outwash region can be observed for the Coupé, as well as for the Sedan, originating from the front wheelarches. The interaction between this flow behavior and the curved bodywork surface prevents the identification of a clear separation line over wheelarches. The tufts placed on the roof surfaces indicate a fully attached flow pattern as expected from CFD.

The effects of the previously mentioned recirculation regions are also visible on the windshields. However, unlike the observations reported in Section 4, a well-defined *A-pillar vortex* is not clearly identifiable in either case, likely

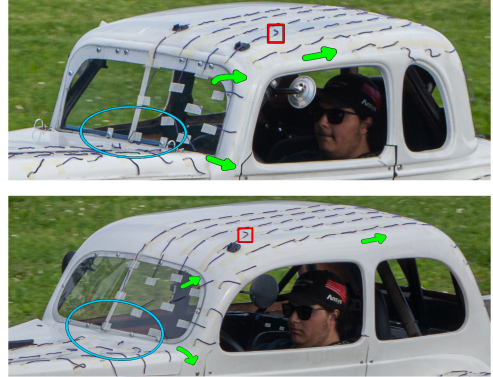


Figure 22: Detail view of the roof and windshield area: Coupé (top) and Sedan (bottom)

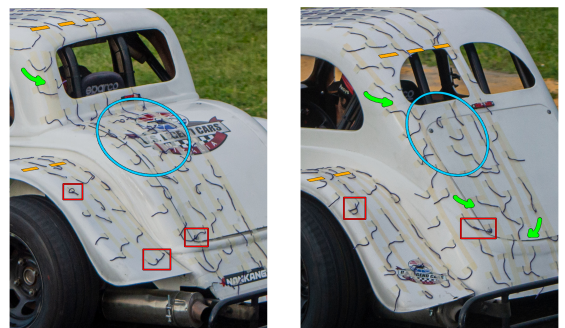


Figure 23: Detail view of the rear sections: Coupé (left) and Sedan (right)

due to the presence of open lateral windows. Shifting now the focus on the rear sections of the Legends Cars, some differences between the Coupé and the Sedan can be spotted.

The flow behind the Coupé is way more chaotic, with larger and less organized recirculation zones, even in the lower part of the wake. The *C-pillar vortex* appears weaker, producing a less intense downwash and exhibiting earlier flow separation, consistent with notchback behavior. Interestingly, the pair of counter-rotating vortices, typical of this configuration flows, is not observed, probably due to the open rear window, which interferes with coherent vortex formation. On the other hand the Sedan exhibits a clearer formed *C-pillar vortex*, drawing the flow downwards as expected in fastback designs. This effect is likely reinforced by the reduced slant angle, which helps maintain flow attachment along the rear surface.

Furthermore, the rear region features a visible recirculation zone, as expected from the geometry. A secondary vortex structure can also be

identified in the central part of the wake, though—similarly to the Coupé—the open rear window configuration negatively impacts the clarity and stability of the flow structures.

Differently from the front wheelarches, the rear ones exhibit a flatter, non-curved geometry, which makes it easier to identify a well-defined separation line.

6. Conclusion

The aerodynamics of the two Legends Cars chassis were analyzed through a numerical study, which highlights the flow field characteristics and reveals notable differences in lift and drag coefficients. Special focus was placed on comparing the flow structures of the two configurations and assessing the aerodynamic impact of adding a simple roof spoiler. Finally, a tuft test was performed to validate some of the CFD results and to evaluate how the geometric simplifications of the numerical model influenced the simulated flow.

The analysis shows that the two chassis generate noticeably different aerodynamic loads, particularly in terms of drag coefficient (C_D), with the Sedan version exhibiting better performance. Although both vehicle chassis are not optimized for aerodynamics, the flow behavior observed in the simulations aligns well with theoretical expectations. Furthermore, the addition of a roof spoiler proves to be effective in reducing drag, especially on the Coupé chassis.

Future developments may include the use of URANS or LES models to better capture unsteady flow phenomena, the investigation of aerodynamic behavior at different operating speeds, the inclusion of additional geometric features such as side mirrors and the direct resolution of the boundary layer instead of simulating it using wall functions.

In summary, this study focused on analyzing the Legends Cars as they are. In fact, it is clear that the use of outdated geometrical designs, with little consideration for aerodynamic efficiency, results in several limitations. Therefore, achieving a significant improvement in aerodynamic performance—as observed, for instance, with the introduction of the roof spoiler—would require substantial modifications to the vehicle geometry.

7. Acknowledgements

The authors wish to thank Adriano Giuseppe Monti and the staff of Castelletto Circuit for kindly providing access to the two Legends Cars used during the tuft test campaign, as well as the track where the tests were conducted.

References

- [1] OpenCFD Ltd. Openfoam - the open source cfd toolbox, 2024. URL <https://www.openfoam.com>.
- [2] B. Blocken, P. Qin, and A. Ricci. CFD simulation of aerodynamic forces on the DrivAer car model: Impact of computational parameters. *Journal of Wind Engineering and Industrial Aerodynamics*, 248:105711, 2024. doi: 10.1016/j.jweia.2024.105711.
- [3] OpenFOAM Foundation. Turbulence modeling: k-omega sst, 2025. URL <https://www.openfoam.com/documentation/guides/latest/doc/guide-turbulence-ras-k-omega-sst.html>.
- [4] Stephen B. Pope. *Turbulent Flows*. Cambridge University Press, 2000. ISBN 9780521598866.
- [5] Wolf-Heinrich Hucho. *Aerodynamics of Road Vehicles*. SAE International, 1998. ISBN 9780768000290.
- [6] See-Yuan Cheng and Shuhaimi Mansor. Influence of rear-roof spoiler on the aerodynamic performance of hatchback vehicle. *MATEC Web of Conferences*, 90:01027, 2017. doi: 10.1051/matecconf/20179001027. URL <https://doi.org/10.1051/matecconf/20179001027>.